

Concept of contrast transfer function for edge illumination x-ray phase-contrast imaging and its comparison with the free-space propagation technique

Paul C. Diemoz,* Fabio A. Vittoria, and Alessandro Olivo

Department of Medical Physics and Biomedical Engineering, University College London, WC1E 6BT London, UK
*p.diemoz@ucl.ac.uk

Abstract: Previous studies on edge illumination (EI) X-ray phase-contrast imaging (XPCi) have investigated the nature and amplitude of the signal provided by this technique. However, the response of the imaging system to different object spatial frequencies was never explicitly considered and studied. This is required in order to predict the performance of a given EI setup for different classes of objects. To this scope, in the present work we derive analytical expressions for the contrast transfer function of an EI imaging system, using the approximation of near-field regime, and study its dependence upon the main experimental parameters. We then exploit these results to compare the frequency response of an EI system with respect of that of a free-space propagation XPCi one. The results achieved in this work can be useful for predicting the signals obtainable for different types of objects and also as a basis for new retrieval methods.

Published by The Optical Society under the terms of the [Creative Commons Attribution 4.0 License](#). Further distribution of this work must maintain attribution to the author(s) and the published article's title, journal citation, and DOI.

OCIS codes: (110.7440) X-ray imaging; (110.2990) Image formation theory; (100.2960) Image analysis.

References and links

1. A. Olivo, F. Arfelli, G. Cantatore, R. Longo, R. H. Menk, S. Pani, M. Prest, P. Poropat, L. Rigon, G. Tromba, E. Vallazza, and E. Castelli, "An innovative digital imaging set-up allowing a low-dose approach to phase contrast applications in the medical field," *Med. Phys.* **28**(8), 1610–1619 (2001).
2. A. Olivo and R. D. Speller, "A coded-aperture technique allowing x-ray phase contrast imaging with conventional sources," *Appl. Phys. Lett.* **91**(7), 074106 (2007).
3. P. R. T. Munro, K. Ignatyev, R. D. Speller, and A. Olivo, "Phase and absorption retrieval using incoherent X-ray sources," *Proc. Natl. Acad. Sci. U.S.A.* **109**(35), 13922–13927 (2012).
4. A. Olivo, S. Gkoumas, M. Endrizzi, C. K. Hagen, M. B. Szafraniec, P. C. Diemoz, P. R. T. Munro, K. Ignatyev, B. Johnson, J. A. Horrocks, S. J. Vinnicombe, J. L. Jones, and R. D. Speller, "Low-dose phase contrast mammography with conventional x-ray sources," *Med. Phys.* **40**(9), 090701 (2013).
5. A. Olivo, P. C. Diemoz, and A. Bravin, "Amplification of the phase contrast signal at very high x-ray energies," *Opt. Lett.* **37**(5), 915–917 (2012).
6. P. C. Diemoz, M. Endrizzi, C. E. Zapata, Z. D. Pešić, C. Rau, A. Bravin, I. K. Robinson, and A. Olivo, "X-ray phase-contrast imaging with nanoradian angular resolution," *Phys. Rev. Lett.* **110**(13), 138105 (2013).
7. P. C. Diemoz, C. K. Hagen, M. Endrizzi, and A. Olivo, "Sensitivity of laboratory based implementations of edge illumination X-ray phase-contrast imaging," *Appl. Phys. Lett.* **103**(24), 244104 (2013).
8. P. C. Diemoz, A. Olivo, M. Endrizzi, and A. Olivo, "On the origin of contrast in edge illumination X-ray phase-contrast imaging," *Opt. Express* **22**(23), 28199–28214 (2014).
9. T. P. Millard, M. Endrizzi, K. Ignatyev, C. K. Hagen, P. R. T. Munro, R. D. Speller, and A. Olivo, "Method for automatization of the alignment of a laboratory based x-ray phase contrast edge illumination system," *Rev. Sci. Instrum.* **84**(8), 083702 (2013).
10. P. C. Diemoz, F. A. Vittoria, and A. Olivo, "Spatial resolution of edge illumination X-ray phase-contrast imaging," *Opt. Express* **22**(13), 15514–15529 (2014).
11. P. R. T. Munro, K. Ignatyev, R. D. Speller, and A. Olivo, "Source size and temporal coherence requirements of coded aperture type x-ray phase contrast imaging systems," *Opt. Express* **18**(19), 19681–19692 (2010).

12. P. R. T. Munro, C. K. Hagen, M. B. Szafraniec, and A. Olivo, "A simplified approach to quantitative coded aperture X-ray phase imaging," *Opt. Express* **21**(9), 11187–11201 (2013).
13. M. Endrizzi, P. C. Diemoz, T. P. Millard, J. L. Jones, R. D. Speller, I. K. Robinson, and A. Olivo, "Hard X-ray dark-field imaging with incoherent sample illumination," *Appl. Phys. Lett.* **104**(2), 024106 (2014).
14. A. Snigireva, I. Snigireva, V. Kohn, S. Kuznetsov, and I. Schelokov, "On the possibility of x-ray phase contrast microimaging by coherent high-energy synchrotron radiation," *Rev. Sci. Instrum.* **66**(12), 5486–5492 (1995).
15. S. W. Wilkins, T. E. Gureyev, D. Gao, A. Pogany, and A. W. Stevenson, "Phase-contrast imaging using polychromatic hard X-rays," *Nature* **384**(6607), 335–338 (1996).
16. Y. I. Nesterets, S. W. Wilkins, T. E. Gureyev, A. Pogany, and A. W. Stevenson, "On the optimization of experimental parameters for x-ray in-line phase-contrast imaging," *Rev. Sci. Instrum.* **76**(9), 093706 (2005).
17. T. E. Gureyev, Y. I. Nesterets, A. W. Stevenson, P. R. Miller, A. Pogany, and S. W. Wilkins, "Some simple rules for contrast, signal-to-noise and resolution in in-line x-ray phase-contrast imaging," *Opt. Express* **16**(5), 3223–3241 (2008).
18. F. A. Vittoria, P. C. Diemoz, M. Endrizzi, L. Rigon, F. C. Lopez, D. Dreossi, P. R. T. Munro, and A. Olivo, "Strategies for efficient and fast wave optics simulation of coded-aperture and other x-ray phase-contrast imaging methods," *Appl. Opt.* **52**(28), 6940–6947 (2013).
19. M. R. Teague, "Deterministic phase retrieval: a Green's function solution," *J. Opt. Soc. Am.* **73**(11), 1434–1441 (1983).
20. R. J. Dejus and M. Sanchez del Rio, "XOP: A Graphical User Interface for Spectral Calculations and X-Ray Optics Utilities," *Rev. Sci. Instrum.* **67**(9), 3356 (1996).
21. K. Li, J. Zambelli, N. Bevins, Y. Ge, and G. H. Chen, "Spatial resolution characterization of differential phase contrast CT systems via modulation transfer function (MTF) measurements," *Phys. Med. Biol.* **58**(12), 4119–4135 (2013).
22. C. K. Hagen, P. Coan, A. Bravin, A. Olivo, and P. C. Diemoz, "A continuous sampling scheme for edge illumination x-ray phase contrast imaging," *J. Appl. Phys.* **118**(5), 054901 (2015).
23. C. Y. Chou and M. A. Anastasio, "Influence of imaging geometry on noise texture in quantitative in-line X-ray phase-contrast imaging," *Opt. Express* **17**(17), 14466–14480 (2009).
24. P. C. Diemoz, A. Bravin, and P. Coan, "Theoretical comparison of three X-ray phase-contrast imaging techniques: propagation-based imaging, analyzer-based imaging and grating interferometry," *Opt. Express* **20**(3), 2789–2805 (2012).
25. Y. I. Nesterets and T. E. Gureyev, "Noise propagation in x-ray phase-contrast imaging and computed tomography," *J. Phys. D Appl. Phys.* **47**(10), 105402 (2014).
26. P. C. Diemoz, M. Endrizzi, C. K. Hagen, C. Rau, A. Bravin, R. D. Speller, I. K. Robinson, and A. Olivo, "Edge illumination X-ray phase-contrast imaging: nanoradian sensitivity at synchrotrons and translation to conventional sources," *J. Phys. Conf. Ser.* **499**, 012006 (2014).

1. Introduction

Edge illumination (EI) X-ray phase-contrast imaging (XPCi) has been developed and investigated during recent years at University College London [1–4]. Besides being applicable at synchrotron radiation (SR) facilities [5,6], EI is naturally suited for laboratory implementations, thanks to its applicability to divergent beams [2], its low coherence requirements [7,8], and the robustness to mechanical and thermal instabilities [9]. Therefore, the technique holds potential for a variety of applications in several fields, including clinical diagnostics.

A number of publications have been dedicated to the modelling of the technique, which were aimed at studying the performance of the technique and its dependence upon the setup parameters (e.g. in terms of sensitivity and spatial resolution) on the one hand [6–8,10,11], and at developing efficient retrieval algorithms on the other [3,6,7,12,13]. However, the response of an EI setup to different object spatial frequencies has not been explicitly studied. A formalism based on the contrast transfer function (CTF), which describes how efficiently each object frequency is transferred to the image, is naturally suited to this scope. In this work, we demonstrate that, under the approximation of near-field regime, a CTF can be defined and calculated for EI. We then exploit this formalism to compare EI with a well-known XPCi technique, free-space propagation (FSP) [14–17], which is currently widely used at both SR facilities and in laboratory setups with microfocal sources.

The next section is dedicated to deriving an analytical expression for the EI CTF, while section 3 validates this approach through a comparison with the full wave optics formalism. An expression for the FSP CTF is obtained in section 4, and subsequently used in section 5 to

compare the performance of EI and FSP. Conclusions are given in section 6. See Table 1 for glossary.

2. Contrast transfer function for edge illumination XPCi

Figure 1 illustrates the working principle of the EI technique. The incoming beam is collimated by a slit of aperture a (henceforth named “pre-sample slit”) before hitting the sample. A second slit of aperture d is placed before the detector (the so-called “detector slit”). This is partially misaligned with respect to the first, so that a fraction of the beam can hit the detector, while the remaining part is stopped. A typical operating condition is represented by the so-called 50% illumination, where half of the beam is absorbed by the slit and the other half is incident on the detector. Assuming the detector aperture is sufficiently large, this condition is realized when one edge of the detector aperture, y_e , is aligned with the centre of the aperture of the sample mask (see Fig. 1). In addition to attenuation, the presence of the object can introduce beam refraction, the latter being proportional to the spatial derivative of the phase shift ϕ through $\Delta\theta_y = \lambda/2\pi \cdot \partial\phi/\partial y$, where λ is the X-ray wavelength. Refraction can alter the proportion between detected and undetected photons. In fact, photons previously incident on the absorbing region of the slit can be deviated onto the detector (increasing the recorded signal), or in the opposite case photons previously counted by the detector can be deviated out (decreasing the recorded signal).

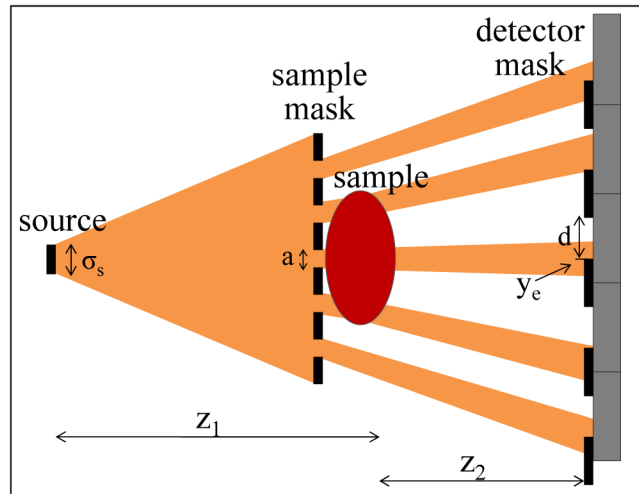


Fig. 1. Schematic diagram of the EI setup when implemented with a conventional X-ray tube (not to scale).

A two-dimensional image is then formed by scanning the sample through the collimated beam, in the direction orthogonal to the slits. When extended beams like those generated by a conventional X-ray tube are used, however, this scan can be avoided, by replacing the slits with masks featuring a plurality of apertures, which replicate the EI principle all over the field of view. The distance between adjacent sampling points, in this latter case, is equal to the period of the pre-sample mask. If higher sampling rate is needed, a procedure known as dithering can be additionally performed: this consists in moving the sample in sub-pixel steps, in acquiring one image at every position, and in combining these to provide a final, more finely sampled image. This procedure leads to increased spatial resolution, down to the intrinsic limit of the imaging system [10]. Since from a point of view of the image signal the “single slit” and “mask” geometries are equivalent (as far as each aperture pair is sufficiently

far from the neighbouring ones, so that they can be considered independent), in the following we will consider the simple case of single sample and detector slits.

If we neglect the direction parallel to the apertures (where the signal is not affected by the presence of the slits [10]), the signal recorded by the detector for each sample scan position p can be written as [18]:

$$S_{EI}(p) = \int_{y_e}^{y_e+d} dy [I_{point}(y; p) * g_{s,p}(y)] \quad (1)$$

i.e. as the integral of the beam intensity falling within the detector aperture region. $g_{s,p}(y)$ represents the projected source intensity distribution, assumed for simplicity to be Gaussian. This is equal to $g_{s,p}(y) = (\sigma_{s,p} \sqrt{2\pi})^{-1} \cdot \exp(-y^2/2\sigma_{s,p}^2)$, where $\sigma_{s,p} = (z_2/z_1) \cdot \sigma_s$, σ_s is the standard deviation of the source intensity distribution, z_1 is the source-to-sample distance and z_2 the sample-to-detector distance.

$$I_{point}(My; p) = M^{-1} I_0 \left[\left[q(y-p) \cdot m(y) \right] * h_{z_{def}}(y) \right]^2 \quad (2)$$

is the intensity (defined as the number of photons per unit length) incident on the detector slit in the case of an ideal point source [18]. I_0 is the intensity incident on the sample mask, $M = (z_1 + z_2)/z_1$ indicates the geometrical magnification and $z_{def} = z_2/M$ is the so-called defocus distance. $h_z(y; \lambda) = [\exp(ikz)/i\lambda z]^{1/2} \exp(iky^2/2z)$ is the one-dimensional Fresnel propagator, where $k = 2\pi/\lambda$ is the wave number. $q(y) = \sqrt{T(y)} \exp(i\phi(y))$ is the object complex transmission function, where T is the transmission, and $m(y) = \text{rect}_a(y)$ is a rectangular function describing the aperture of the sample mask, defined as 1 in the range $[-a/2, a/2]$ and 0 elsewhere.

In recent work [8], we demonstrated how the full wave optics treatment (represented by Eqs. (1) and (2)) can be substantially simplified in the case of near-field regime, if the well-known transport of intensity equation (TIE) is used to approximate the intensity incident on the detector mask [19]. The TIE, which has been used extensively in the framework of FSP, is valid for sufficiently small propagation distances and sufficiently slowly varying object structures (i.e. for limited object spatial frequency) [17].

In particular it was found that, under these assumptions, the transmission and refraction signals can be calculated simply as a convolution between the relevant object property and appropriate point spread functions (PSF), i.e [8]:

$$S_{EI}(p) = I_0 [T * f_T](p) + I_0 k^{-1} \left[T \frac{\partial \phi}{\partial y} * f_R \right](p) \quad (3)$$

where f_T and f_R are the position-dependent transmission and refraction sensitivity functions, respectively, which depend on the setup geometry through:

$$f_T(y) = [g_{s,r} * \text{rect}_{d/M}](y + y_e/M + d/2M) \cdot \text{rect}_a(y) \quad (4)$$

$$f_R(y) = [g_{s,r}(y_e/M + y) - g_{s,r}(y_e/M + d/M + y)] \cdot z_{def} \text{rect}_a(y) \quad (5)$$

$rect_{d/M}(y - y_e/M - d/2M)$ represents the detector aperture, while $g_{s,r}(y) = (1/\sigma_{s,r}\sqrt{2\pi}) \cdot \exp(-y^2/2\sigma_{s,r})$ is the projected source distribution rescaled back to the object plane, with $\sigma_{s,r} = z_2/(z_1 + z_2) \cdot \sigma_{s,p}$. Equations (3)-(5) will be the central focus of this work.

In Fig. 2(a), we report examples of transmission and refraction sensitivity functions $f_T(y)$ and $f_R(y)$, for a typical EI laboratory configuration. The following parameters were considered: $z_1 = 1.6$ m, $z_2 = 0.4$ m, source FWHM = 70 μm , $a = 20$ μm , $d = 40$ μm , and a 50% misalignment between sample and detector apertures (corresponding to the detector aperture edge being aligned with the centre of the sample aperture, i.e. a position $y_e = 0$). The two functions plotted in Fig. 2(a) represent the different weight of the various points within the illuminated region, in terms of producing the transmission and refraction signals on the image, respectively. As expected, the maximum weight for the refraction signal corresponds to the edge position y_e [8]. In Fig. 2(b), we report a typical signal profile obtained using the above TIE approach (Eqs. (3)-(5)) for a cylindrical object of 200 μm diameter. It can be seen that the edges of the object are highlighted by the positive and negative peaks due to refraction, while the object absorption produces a slight decrease of the measured signal within the wire.

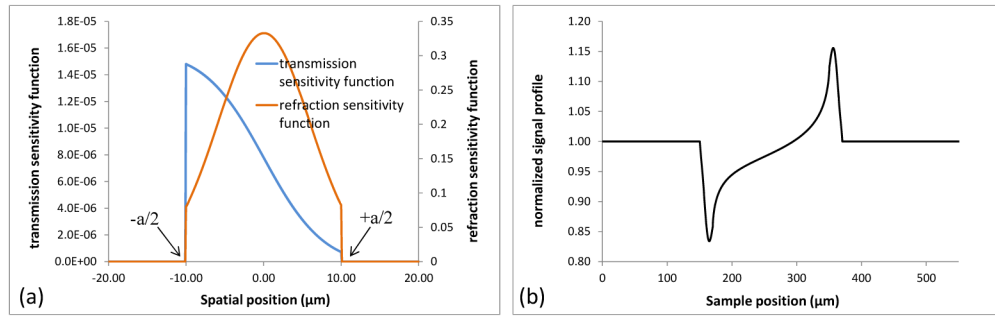


Fig. 2. (a) Examples of transmission and refraction sensitivity functions $f_T(y)$ and $f_R(y)$. (see text for the considered experimental parameters). (b) Example of EI signal measured in the case of a cylindrical object producing both absorption and refraction.

Since we are mainly interested in determining how the phase contrast (rather than the attenuation contrast) varies at different spatial frequencies, we will consider here the case of a pure phase object. Equation (3) then reduces to:

$$S_{EI}(p) = I_0 F_T + I_0 k^{-1} \left[\frac{\partial \phi}{\partial y} * f_R \right](p) \quad (6)$$

where $F_T \equiv \int_{-\infty}^{\infty} dy f_T(y)$ is the so-called integral sensitivity function for the transmission signal.

The image contrast for EI is then equal to:

$$C_{EI}(p) \equiv \frac{S_{EI}(p) - S_{EI,ref}}{S_{EI,ref}} = F_T^{-1} k^{-1} \left[\frac{\partial \phi}{\partial y} * f_R \right](p) \quad (7)$$

where $S_{EI,ref} \equiv S_{EI}(\partial \phi / \partial y = 0)$ is the signal recorded when no object is present in the beam. If the Fourier transform of both sides of Eq. (7) is taken, this convolution operation can be converted into a simple product, i.e.:

$$F\{C_{EI}\} = F_T^{-1} k^{-1} 2\pi i f_y F\{f_R\} \cdot F\{\phi\} = CTF_{EI}(f_y) \cdot F\{\phi\} \quad (8)$$

where f_y is the spatial frequency along y , and where we have introduced a CTF for EI. The Fourier transform of the image contrast is thus simply equal to the product between the Fourier transform of the phase shift introduced by the object and the function $CTF_{EI}(f_y)$. The latter function expresses how well each spatial frequency is transferred from the object to the image, and is thus very useful to estimate the performance of a given setup for different types of samples.

Note that, in general, the refraction sensitivity function $f_R(y)$ is not symmetric (see Eq. (5) and Fig. 4(b) in [8]). This, in turns, means that its Fourier transform is in general a complex function. However, we can make two simplifying approximations (which are quite easily satisfied in practice): 1) the detector aperture is larger than the beam incident on it, 2) a typical 50% illumination is considered. Under these conditions, the refraction sensitivity function can be approximated as:

$$f_R(y) = g_{s,r}(y) \cdot z_{def} rect_a(y) \quad (9)$$

and is thus even. Therefore, its Fourier transform is also even and real. Since in this case $F_T = a/2$, the CTF is now equal to:

$$CTF_{EI}(f_y) = 4i\pi a^{-1} k^{-1} f_y F\{f_R\} \quad (10)$$

Note that a purely imaginary CTF implies that the signal profile is shifted by one fourth of a period compared to the original phase profile (since a multiplication by ‘i’ in Fourier space corresponds to a shift of $(4f_y)^{-1}$ in real space). If we take into account a sinusoidal phase profile, in fact, the maximum signal is not obtained at the position where the phase is maximum (at the peak of the sinusoid), but at the one where the refraction angle is (i.e. at the flank of the sinusoid). The explicit expression of the CTF can be obtained by developing the Fourier transform of the refraction sensitivity function:

$$CTF_{EI}(f_y) = 4i\pi a^{-1} k^{-1} z_{def} f_y [F\{g_{s,r}\} * F\{rect_a\}](f_y) = 4i\pi a^{-1} k^{-1} z_{def} f_y \cdot \left[\frac{\sin(\pi f_y)}{\pi f_y} \right] * \left[\exp(-2\sigma_{s,r}^2 \pi^2 f_y^2) \right] \quad (11)$$

The CTF depends in a complicated way on the acquisition parameters, and in particular on the source blurring $\sigma_{s,r}$ and on the frequency f_y . However, it is possible to study its behaviour in some limit cases, such as at low and high frequencies.

In the case of low frequencies, the Fourier transform of the refraction sensitivity function tends to $F\{f_R\}(f_y = 0) = \int dy f_R(y) \equiv F_R$, where F_R is the so-called integral sensitivity function for refraction [8]. The latter quantity was shown to be equal to [8]:

$$F_R = z_{def} \int_{-Ma/2}^{Ma/2} dy g_{s,r}(y) = z_{def} Ma \frac{\partial Ic}{\partial y_e} \quad (12)$$

where $Ic = F_T/a$ is the so-called illumination curve [6]. Therefore, at low frequencies the CTF tends to:

$$CTF_{EI}(f_y) = 4i\pi k^{-1} f_y M z_{def} \frac{\partial Ic}{\partial y_e} \quad (13)$$

and is thus proportional to the spatial frequency. By combining Eqs. (8) and (13), and noticing that $F\{\Delta\theta_y\} = 2\pi i f_y k^{-1} F\{\phi\}$, we see that:

$$C_{EI}(p) = z_2 \frac{1}{Ic} \frac{\partial Ic}{\partial y_e} \Delta\theta_y(p) \quad (14)$$

Equation (14) agrees with the expression obtained for the contrast in [6,7], if a linear approximation of the illumination curve is considered. This is not surprising: in fact, the refraction angle was assumed to be constant within the size of the sample aperture in [6,7], which indeed amounts to the same assumption of low object spatial frequencies employed to derive Eqs. (12)-(14).

In the opposite case of high frequencies, instead, it can be proven numerically using Eq. (11) that the CTF does not converge to a constant value but keeps on oscillating around zero, with a constant amplitude (see also simulations in next section). In order to understand why the CTF does not converge despite the presence of source blurring, we need to remember that, in the expression for the refraction sensitivity function f_R (Eq. (5)), the source blurring function multiplies (in real space) the rectangular function representing the pre-sample aperture. Thus, source blurring does not reduce the high frequencies content of f_R , as the sharp cut-off imposed by the pre-sample aperture is still present. On the contrary, the larger the source blurring, the larger is the step on the two sides of f_R (see Fig. 2(a)) and thus the higher the CTF at high frequencies. However, this is not the case if the perfectly sharp mask apertures considered until now are replaced with mask apertures with smooth edges. This can be considered analytically by replacing, in Eq. (9), $rect_a(y)$ with $rect_a(y) * g_{ap}(y)$ and $g_{s,r}(y)$ with $g_{s,r}(y) * g_{ap}(My)$, where $g_{ap}(y)$ is a function that defines the smoothing of the edge transmission function (for simplicity here considered a Gaussian) [8]. We will see in the next section that this has the direct effect of damping high frequencies in the image, while leaving low frequencies almost unaffected.

3. Comparison with full wave optics formalism

In order to qualitatively evaluate the agreement between the CTF and wave optics formalisms, and appreciate the range of validity of the former, we carry out the following simulations. An object with sinusoidal phase profile $\phi(y) = \phi_{\max} \sin(2\pi f_y y)$ is considered. The signal profile $S_{EI}(p)$ is calculated through wave optics, using the code described in [18], for a wide range of object frequencies. The signal profile shows an oscillating trend, due to the input sinusoidal shape of the object. Examples of input phase profile and corresponding signal obtained using wave optics are reported in Fig. 3(a), in the case of a sinusoidal nylon object with 30 μm maximum thickness and 30 μm period. The following experimental parameters typical of laboratory implementations of EI were considered: $z_1 = 1.6$ m, $z_2 = 0.4$ m, source FWHM = 70 μm , pixel size = 100 μm , $a = 20$ μm , $d = 40$ μm , $E = 40$ keV (refractive index of nylon at this energy is $\delta = 1.67 \cdot 10^{-7}$ [20]). Mask edges are assumed to be perfectly sharp. A very small dithering step (0.1 μm) is used in the simulations, in order to exclude any artefact due to undersampling (e.g. aliasing). We see that a shift is present between the phase and signal profiles, as the maximum signal arises where the refraction angle (proportional to the first derivative of the phase profile), and not the phase itself, assumes its maximum value.

At each frequency, the quantity $C_{EI,\max}/\phi_{\max}$, where $C_{EI,\max}$ is the peak contrast of the oscillating signal profile obtained using wave optics, can be calculated and compared with the absolute value of the CTF obtained in the near-field approximation (Eqs. (10)-(11)). Note that $|CTF|$ effectively represents the (phase) modulation transfer function of the imaging system

[21]. $|CTF|$ profiles calculated with TIE and wave optics approaches are compared in Figs. 3(b) and 3(c), in the case of sinusoidal nylon objects of maximum thickness of 1 μm and 50 μm , respectively. The profiles oscillate as a function of the frequency and, as predicted in previous section for the TIE case, do not converge to zero at high frequencies. It can be seen from inspection of Eq. (5) that, in the approximation of very large source blurring, the refraction sensitivity function f_R becomes a rectangular function. Therefore, according to Eq. (11), the positions of the maxima of the $|CTF|$ correspond to the points $f_y = (2a)^{-1} + na^{-1}$, with $n = 0, 1, 2, \dots$, where the modulus of the sinus function is maximized. The minima, instead, correspond to $f_y = a^{-1}(n+1)$, where the sinus function is equal to zero. Intuitively, this can be understood by noting that, if the object period is a submultiple of the aperture size, half of the illuminated object refracts towards the detector aperture, and the other half towards the area covered by the detector mask, thus resulting in a contrast equal to zero. $f_{y,0} = (2a)^{-1}$, corresponding to the first maximum, can be considered as a fundamental frequency of the setup (note it is only dependent on the sample mask aperture). It separates, in fact, the low-frequency region where the CTF is proportional to the frequency (approximation considered in [6,7] and shown here in Eq. (13)) from the high-frequency region where the CTF has an oscillating behaviour. Note also that, up to the first zero of the CTF at $2f_{y,0}$, the contrast maintains always the same sign. Every zero-crossing of the plot corresponds, however, to a contrast inversion in the image (this is better seen in profiles of CTF in Fig. 5(a)).

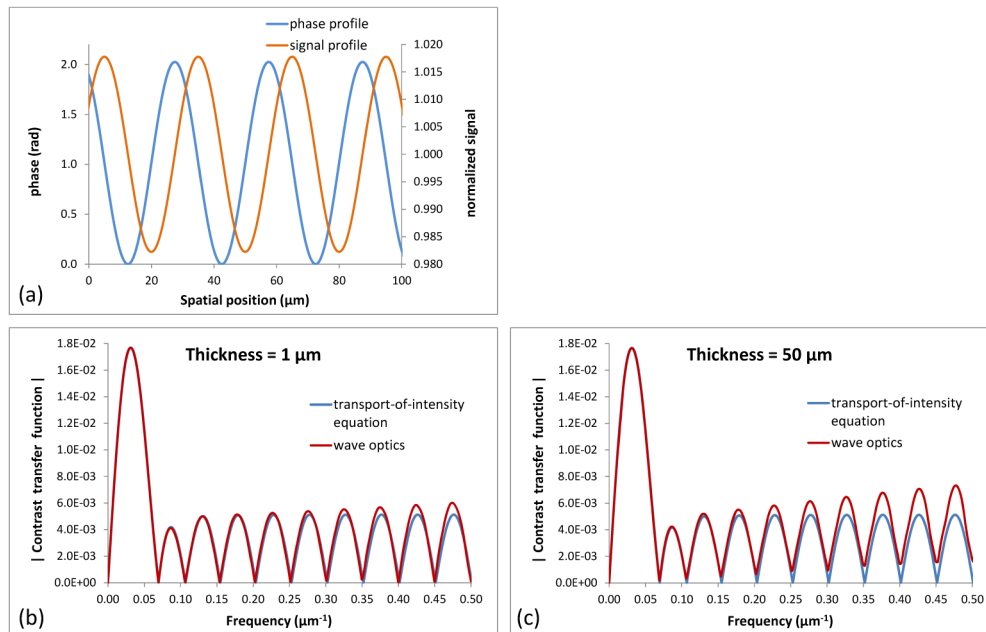


Fig. 3. (a) Phase and signal profiles for a sinusoidal nylon object with 30 μm maximum thickness at 40 keV, calculated using rigorous wave optics (see text for details on experimental parameters). Comparison between $|CTF|$ calculated in near-field approximation and the corresponding quantity from wave optics simulations, for: a) maximum object thickness of 1 μm , b) maximum object thickness of 50 μm .

In our example, the source blurring is not very large and, as a consequence, the positions of the maxima and minima are shifted by a few μm with respect to the values calculated above in the approximation of very large source blurring. However, the same behaviour holds,

with the $|CTF|$ oscillating at high frequencies without converging to zero. It can be seen that, at low and intermediate frequencies, there is perfect agreement between the wave optics and the CTF formalisms, highlighting the validity of our approach. The two profiles, however, become increasingly different at high frequencies, as expected. This is due to diffraction effects not accounted for by the TIE formalism (which is indeed based on geometrical optics). It can also be noted that the level of disagreement is different for the two object thicknesses. As predicted in [8], in fact, the accuracy of the TIE formalism improves not only for decreasing frequencies, but also for smaller signal amplitudes. The effect of energy is also noteworthy: it can be shown (data not reported here), in fact, that the accuracy of the TIE approximation improves at high x-ray energies and becomes worse at low x-ray energies, as in the latter case diffraction effects are larger.

The above simulations considered a fixed object thickness. However, in some cases it might be more useful to assume the object thickness and spatial frequency to be related, for instance as $thickness = f_y^{-1}$. In fact, at least for some classes of objects (such as cylindrical or spherical, like certain structures encountered in biological tissues), it is reasonable to assume that object details that are thin along the beam direction will also contain a larger proportion of high frequencies in the transverse direction. Note that this is equivalent to assuming a fixed refraction angle, as this is proportional to the first derivative of the phase and thus to $thickness \cdot f_y$. This case is represented by simulations reported in Fig. 4(a). The agreement between wave optics and TIE profiles is improved compared to the case of a fixed object thickness of 50 μm , as the simultaneous presence of large object thicknesses and high frequencies is avoided.

Until now we have considered the case of ideal, perfectly sharp mask apertures. However, the masks will in practice exhibit some degree of smoothing which, in turn, will tend to wash out the high frequencies. In order to show the importance of this effect, the profiles shown in Fig. 3(c) (maximum object thickness of 50 microns) are repeated for smooth apertures in Fig. 4(b). The standard deviation of the Gaussian function describing the edge smoothing was assumed to be equal to 1 μm . Low frequencies are not affected by this smoothing, while high frequencies quickly vanish, leading to significantly improved agreement between the two profiles.

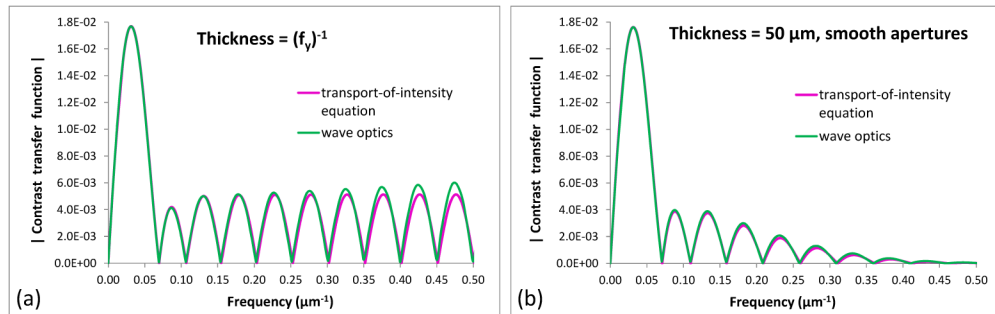


Fig. 4. Comparison between $|CTF|$ calculated in near-field approximation and the corresponding quantity from wave optics simulations (laboratory setup, see text for details): a) in the case of a maximum object thickness dependent on the frequency, with $thickness = f_y^{-1}$, b) in the case of a fixed maximum object thickness of 50 μm , but with smoothed mask apertures ($\sigma_{ap} = 1\mu\text{m}$).

A few words need also to be spent on the effect of sampling. In the simulations presented above, a very small dithering step was considered, thus providing the CTF obtainable in ideal

conditions. In a practical experimental situation, however, the ideal signal profile (expressed by Eq. (3)) is only sampled in a finite number of points, with the distance between adjacent points in the final image being given by the period of the sample mask (or by the dithering step, if the dithering procedure is performed). This might give rise to so-called aliasing artefacts. In order to ensure that this effect does not take place, one should use a dithering step smaller than $1/(2f_{max})$, where $f_{max} = \min(f_o, f_i)$, f_o is the largest non-negligible frequency in the object, and f_i is the largest non-negligible frequency of the imaging system CTF. A detailed analysis on the effects of aliasing for EI, as well as an efficient strategy to eliminate them, are presented in [22].

4. Contrast transfer function for free-space propagation XPCi

In analogy with what done for EI in section 2, we will consider here the case of the near-field regime. Under this condition, the TIE can be used to approximate the intensity incident on the detector as [17,19]:

$$I_{FSP}(y) = [I_{FSP,point} * g_{s,p}](y) \quad (15)$$

The function $g_{s,p}$, defined in section 2, is the projected source intensity distribution, assumed to be Gaussian. $I_{FSP,point}$ represents the intensity obtained with a point source, which is equal to [17,19]:

$$I_{FSP,point}(My) = M^{-1}I_0T(y) - M^{-1}I_0k^{-1}z_{def}T(y)\frac{\partial^2\phi}{\partial y^2}(y) \quad (16)$$

where I_0 is the intensity incident on the sample. Note that, in the above equation, we have made the assumption of slowly varying object attenuation, which enables us to neglect the phase-attenuation cross term in the TIE.

The signal recorded at each detector pixel position p can then be expressed as a convolution of the FSP intensity with the pixel response function:

$$S_{FSP}(p) = [I_{FSP} * f_{det}](p) \quad (17)$$

We will assume in the following that the detector point-spread function is of the form:

$$f_{det}(y) = [g_d * rect_{\Delta p}](y) \quad (18)$$

where $g_d(y)$ indicates a normalized Gaussian function of standard deviation σ_d , and $rect_{\Delta p}(y)$ is a rectangular function of width equal to the pixel size Δp , which is defined as 1 in the range $[-\Delta p/2, \Delta p/2]$ and 0 elsewhere. The Gaussian function expresses a possible blurring of the beam by the detector components (such as a scintillator, for instance), while the rectangular function expresses the subsequent binning process in the different detector pixels.

Combining Eqs. (15)-(18), and assuming the transmission function to be approximately constant within each pixel, gives:

$$S_{FSP}(p) = I_0\Delta pM^{-1}T(p) - I_0k^{-1}z_{def}T(p)\left[\frac{\partial^2\phi}{\partial y^2} * f_{s,d}\right](p) \quad (19)$$

where $f_{s,d}(y) = [g_{s,r} * g_{d,r} * \text{rect}_{\Delta p/M}](y)$ is the combined source-detector point-spread function referred to the object plane coordinates, and $g_{d,r}$ is a normalized Gaussian function of standard deviation σ_d/M .

Consistently with what done for EI, we consider here the case of no object absorption. The image contrast is then equal to:

$$C_{FSP}(p) \equiv \frac{S_{FSP}(p) - S_{FSP,ref}}{S_{FSP,ref}} = -k^{-1} M \Delta p^{-1} z_{def} \left[\frac{\partial^2 \phi}{\partial y^2} * f_{s,d} \right](p) \quad (20)$$

where $S_{FSP,ref} \equiv S_{FSP}(\partial^2 \phi / \partial y^2 = 0)$ is the signal recorded with no object in the beam. Taking the Fourier transform of both sides of Eq. (20) allows transforming the convolution operation into the following product:

$$F\{C_{FSP}\} = -k^{-1} M \Delta p^{-1} z_{def} 4\pi^2 f_y^2 F\{\phi\} \cdot F\{f_{s,d}\} = CTF_{FSP}(f_y) \cdot F\{\phi\} \quad (21)$$

where we have introduced the following CTF for FSP:

$$CTF_{FSP}(f_y) \equiv -k^{-1} M \Delta p^{-1} z_{def} 4\pi^2 f_y^2 F\{f_{s,d}\} \quad (22)$$

By developing the Fourier transform of the FSP system response function in Eq. (22), we can rewrite the CTF as:

$$CTF_{FSP}(f_y) = -k^{-1} M \Delta p^{-1} z_{def} 4\pi f_y \sin(\pi f_y \Delta p M^{-1}) \cdot \exp[-2(\sigma_{d,r}^2 + \sigma_{s,r}^2) \pi^2 f_y^2] \quad (23)$$

It is useful to note that, at low frequencies, $CTF_{FSP} \propto f_y^2$, as a direct consequence of the fact that contrast in FSP is proportional to the second spatial derivative of the phase. Thus, CTF_{FSP} is equal to zero at $f_y = 0$. At high frequencies, CTF_{FSP} also goes to zero, due to the damping effect of the exponential, representing the loss of spatial resolution due to the imaging system.

Like for the EI technique, also for FSP the problem of aliasing might arise. In fact, in a practical experiment, the signal (expressed by Eq. (19)) is only sampled in a finite number of points p : in this case, the distance between adjacent points is equal to the demagnified pixel size, i.e. $\Delta p/M$. In order to ensure that this effect does not take place, like for EI, the sampling rate should be higher than $2f_{max}$, where $f_{max} = \min(f_o, f_i)$, f_o is the largest non-negligible frequency in the object, and f_i is the largest non-negligible frequency of the imaging system CTF. It is worth mentioning that a procedure similar to dithering in EI could be adapted to the case of FSP, whereby the sample is scanned in sub-pixel steps and multiple images are acquired and combined. This would enable correctly capturing the various object frequencies, and eliminate possible aliasing artefacts.

5. Comparison between EI and FSP transfer functions

We can now proceed to calculate the ratio between the EI and FSP contrast transfer functions, as a function of spatial frequency. Not only does this allow comparing the amplitude of the signals in the two techniques, but also how different object spatial frequencies are transferred to the image in the two cases.

Using Eqs. (10)-(11) and (22)-(23), this ratio can be written, for perfectly sharp masks, as:

$$\frac{CTF_{EI}}{CTF_{FSP}}(f_y) = \frac{ia^{-1}F\{f_R\}}{-M\Delta p^{-1}z_{def}\pi f_y F\{f_{s,d}\}} = -\frac{i\Delta p \cdot \left[\frac{\sin(\pi a f_y)}{\pi f_y} \right] * \left[\exp(-2\sigma_{s,r}^2 \pi^2 f_y^2) \right]}{aM \sin(\pi f_y \Delta p M^{-1}) \cdot \exp[-2(\sigma_{d,r}^2 + \sigma_{s,r}^2) \pi^2 f_y^2]} \quad (24)$$

We first note that, within the near-field approximation considered here, the two CTFs are only dependent on the geometrical parameters of the employed setups and on the frequency, while they are independent of energy. This comes directly from the fact that the near-field approximation is based on geometrical optics. The expression in Eq. (24) and its dependence upon the various parameters is rather complicated. However, it is possible to identify some interesting limiting cases. In particular, it is instructive to look at the effect of low and high spatial frequencies.

At low frequencies, we can exploit the result obtained in Eq. (12) for $F\{f_R\}$ to get, from Eq. (24):

$$\frac{CTF_{EI}}{CTF_{FSP}}(f_y) = -\frac{i\Delta p \cdot \partial I_c / \partial y_e}{\sin(\pi f_y \Delta p M^{-1})} \square -i\pi^{-1} f_y^{-1} M \frac{\partial I_c}{\partial y_e} \quad (25)$$

It is easy to see that, for frequencies tending to zero, the modulus of this ratio tends to infinite. This means that the amplitude of the EI signal is much larger than the FSP one at low frequencies. Note that this follows directly from the fact that, to first approximation, EI contrast is proportional to the first derivative of the phase, while FSP contrast is proportional to its second derivative.

In the opposite case of high frequencies, the ratio also goes to infinite, as the denominator quickly goes to zero due to the exponential, while it can be shown numerically that the numerator only goes to zero as f_y^{-1} . Whether this range of frequency is relevant in a given experimental situation will ultimately depend on both the sample (whether it contains structures with significant high frequencies) and on the level of stochastic noise in the image. Signals at these frequencies, in fact, are typically smaller in amplitude and will be measurable only if they are larger than the noise level. For intermediate frequencies, the value of the ratio between the two CTFs assumes finite values larger or smaller than 1, depending on the chosen parameters.

If smooth mask edges are considered, however, Eq. (24) is rewritten as:

$$\frac{CTF_{EI}}{CTF_{FSP}}(f_y) = -\frac{i\Delta p \cdot \left[\frac{\sin(\pi a f_y)}{\pi f_y} \cdot \exp(-2\sigma_{ap}^2 \pi^2 f_y^2) \right] * \left[\exp(-2(\sigma_{s,r}^2 + M^{-2}\sigma_{ap}^2) \pi^2 f_y^2) \right]}{aM \sin(\pi f_y \Delta p M^{-1}) \cdot \exp[-2(\sigma_{d,r}^2 + \sigma_{s,r}^2) \pi^2 f_y^2]} \quad (26)$$

where σ_{ap} represents the smoothing of the transmission function of both the sample and detector masks. Since typically $M^{-1}\sigma_{ap} \square \sigma_{s,r}$, the effect on the low frequencies is negligible. Moreover, even if high frequencies are affected by the mask smoothing, the ratio between CTFs still goes to infinite as in the case of sharp apertures, since typically $\sigma_{ap} \square \sqrt{\sigma_{d,r}^2 + \sigma_{s,r}^2}$.

Another interesting aspect to consider is the dependence on different system spatial resolutions. If the detector resolution is high ($\Delta p \rightarrow 0$ and $\sigma_{d,r} \rightarrow 0$) and the source blurring is small ($\sigma_{s,r} \rightarrow 0$) (but the geometrical optics approximation can still be used), then the ratio between EI and FSP CTFs goes to zero, i.e. FSP provides much larger signals than EI. Conversely, for large pixel sizes and large source blurring, the ratio tends to infinite as the

FSP signal decreases very rapidly. This is not surprising, as it is well known that FSP is highly sensitive to changes in the system spatial resolution [23–25].

The effect of sampling should also be taken into account. As mentioned in previous sections, in fact, the CTF approach implicitly assumes that the sampling rate is sufficiently high to prevent aliasing artefacts [22]. As we have seen, the necessary sampling rate will depend on both the frequency content of the imaging system CTF and the frequency content of the sample itself. The sampling rate is determined by the mask period for EI and by the pixel size for FSP, but for both techniques it can be artificially improved by introducing an additional scan of the object (in the case of EI, this procedure is known as dithering). However, this additional scan inevitably leads to longer acquisition times and higher doses to the sample, as a larger number of frames needs to be acquired.

In the following, we will present calculations of CTFs for a range of different spatial frequencies, in order to exemplify the above findings. For EI, we consider the following experimental parameters, corresponding to typical laboratory implementations of the technique: $z_1 = 1.6\text{m}$, $z_2 = 0.4\text{m}$, source FWHM = $70\ \mu\text{m}$, $d = 40\ \mu\text{m}$, $\sigma_{ap} = 0.5\ \mu\text{m}$ (note that the contrast is independent of the pixel size, as long as cross-talk between two adjacent apertures is avoided). In Fig. 5(a), we show CTF profiles obtained using different sample aperture sizes: $a = 15\ \mu\text{m}$, $20\ \mu\text{m}$, and $30\ \mu\text{m}$. The plots clearly show the strong dependence of the CTF upon the sample aperture. The overall amplitude of the CTF is modified, with smaller apertures corresponding to higher contrast. This agrees with previous findings obtained considering only the case of low frequencies [26]. Moreover, also the position of the minima and maxima is changed: for instance, the main maximum is shifted towards higher frequencies when the aperture size is decreased. Extrapolation for smaller aperture sizes than those presented here, however, should be done with care. It is expected, in fact, that TIE will lose accuracy for smaller aperture sizes, and as a result the real contrast improvement will be inferior to that predicted by TIE. Moreover, the use of small sample apertures reduces the flux on the sample and detector, thus requiring an increase in the exposure time to compensate for the decrease in the photon statistics. Therefore, an optimal value for the aperture is expected to exist, depending on the specific application.

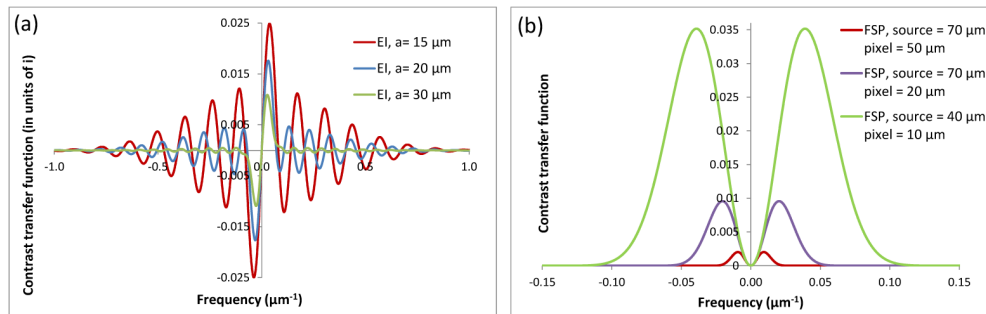


Fig. 5. CTFs calculated for different XPCi laboratory setups: a) EI with sample aperture sizes of 15, 20 or $30\ \mu\text{m}$ (see text for the values of the other experimental parameters), b) FSP with different source-detector combinations: source FWHM = $70\ \mu\text{m}$ and pixel size = $50\ \mu\text{m}$, source FWHM = $70\ \mu\text{m}$ and pixel size = $20\ \mu\text{m}$, source FWHM = $40\ \mu\text{m}$ and pixel size = $10\ \mu\text{m}$ (see text for the values of the other experimental parameters).

In Fig. 5(b), we show curves obtained for FSP. The same distances $z_1 = 1.6\ \text{m}$ and $z_2 = 0.4\ \text{m}$ are used. Three different cases are considered: i) source FWHM = $70\ \mu\text{m}$, pixel size = $50\ \mu\text{m}$, ii) source FWHM = $70\ \mu\text{m}$, pixel size = $20\ \mu\text{m}$, iii) source FWHM = $40\ \mu\text{m}$, pixel size = $10\ \mu\text{m}$. In all three cases, the detector PSF is modelled as a box function (of width equal to the pixel size) convolved with a Gaussian function of standard deviation σ_d equal to half the pixel size. By examining the plots, we can see that the CTF is always equal to 0 at $f_y = 0$

(due to the dependence of the contrast upon the second derivative of the phase), and goes to zero again, rapidly, at high frequencies (due to the finite spatial resolution of the system). Moreover, as expected, the CTF is strongly dependent on the spatial resolution of the imaging system, determined by the source size and the detector PSF. Higher spatial resolution corresponds to higher image contrast, and also to a shift of the CTF peak towards higher frequencies. However this comes with a price, in particular lower photon flux (if a small source is used) and smaller field of view (for a small pixel size). We also would like to note that the arrangement here presented for FSP is not necessarily an optimized one, and has just been chosen for illustrative purposes. Comprehensive studies on the optimization of a FSP setup, depending on the required spatial resolution and contrast, can be found in the literature (see, for instance [16,17,24,25]).

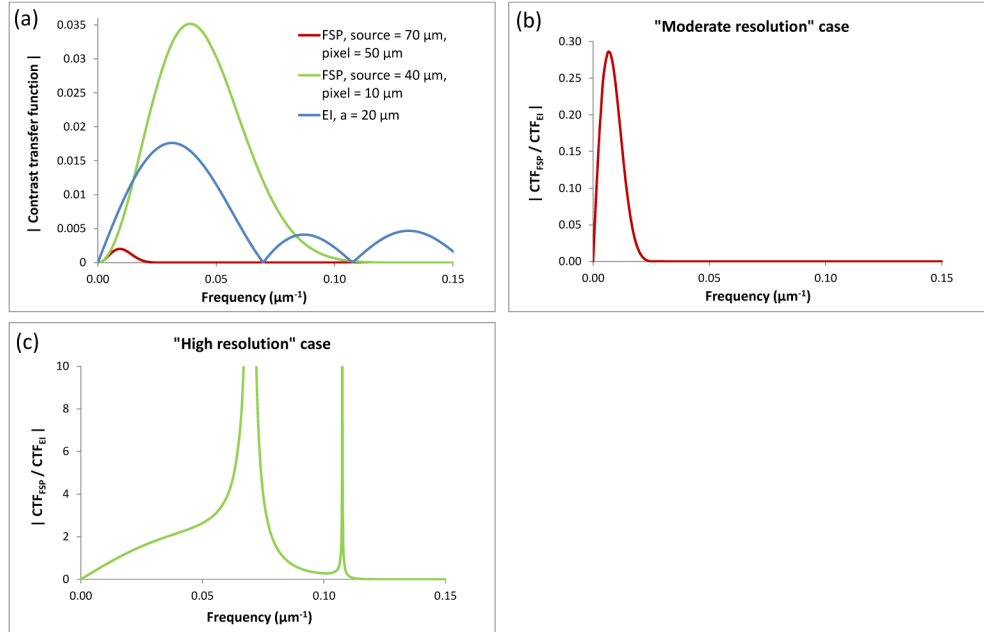


Fig. 6. Comparison of EI and FSP CTFs. a) EI setup with source FWHM = 70 μm and sample aperture = 20 μm sample aperture, “moderate resolution” FSP setup with source FWHM = 70 μm and pixel size = 50 μm , “high resolution” FSP setup with source FWHM = 40 μm and pixel size = 10 μm . b) Ratio $|CTF_{FSP} / CTF_{EI}|$ in the case of the “moderate resolution” FSP setup. c) Ratio $|CTF_{FSP} / CTF_{EI}|$ in the case of the “high resolution” FSP setup. Note that, in the latter plot, the two peaks correspond to the zeros of CTF_{EI} .

In Fig. 6(a), we compare $|CTF|$ profiles for the two techniques in a few selected cases: i) the “moderate resolution” FSP setup with source FWHM = 70 μm and pixel size = 50 μm , ii) the “high resolution” FSP setup with source FWHM = 40 μm and pixel size = 10 μm , and iii) the EI setup with FWHM = 70 μm , $a = 20 \mu\text{m}$. Since these profiles are symmetric with respect to $f_y = 0$, only positive frequencies are shown in the graph. Plots of $|CTF_{FSP} / CTF_{EI}|$, obtained considering either the moderate resolution or the high resolution FSP setups, are shown in Figs. 6(b) and 6(c), respectively. We see that, in a system with low/moderate spatial resolution, EI outperforms FSP at all frequencies ($|CTF_{FSP} / CTF_{EI}|$ is always less than 1). In order to achieve higher contrast than EI, a high-resolution system for FSP is needed. We need to note that, in this case, FSP also presents an advantage in terms of sampling with respect to EI. In fact, the same sampling rate necessary to avoid aliasing artefacts might be achieved in

one exposure using a small pixel size in FSP, but might require the acquisition of several frames (dithering procedure) for an EI system featuring a large mask period. For these reasons, a spatial resolution threshold therefore appears to exist, at which the signals provided by the two techniques are comparable: at values smaller than this, FSP gives the highest signal, while at larger values EI prevails. Besides providing larger signals for moderate system spatial resolution, EI also gives larger signals for low object frequencies, since the CTF goes to zero as $CTF_{EI} \propto f_y$ while $CTF_{FSP} \propto f_y^2$. This further confirms that EI might be more suited for imaging larger samples, while FSP might be advantageous for smaller ones.

6. Conclusions

We have developed the concept of a contrast transfer function for EI XPCi, under the geometrical optics approximation. The validity of this approach has been confirmed by comparison with more rigorous wave optics calculations. The agreement between the geometrical and wave optics methods depends on the experimental setup under consideration and on the object itself. In particular, it improves for high X-ray energies, larger mask apertures, larger source blurring, smaller phase variations in the sample and lower spatial frequencies.

The expression obtained for the EI CTF was used to study the influence of the various experimental parameters. The CTF also enables estimating the contrast in the cases of both low and high object spatial frequencies. It was found that, at low frequencies, the CTF is proportional to the spatial frequency, which implies that the image contrast is proportional to the first derivative of the phase, or equivalently to the refraction angle. This agrees with previous models for phase retrieval in EI [6,7,13]. However, the situation is very different at high frequencies: the CTF does not grow linearly but, after a certain threshold frequency, it shows an oscillating behaviour. Since previous retrieval algorithms do not take this effect into account, they are prone to underestimating the high frequency components of the phase, effectively resulting in a blurring of the retrieved phase profile compared to the “true” one. The CTF should be taken into account for the correct quantitative retrieval of refraction angles generated by high frequency phase variations within the object.

The expression for the EI CTF was then used to compare the frequency response of the EI and FSP XPCi techniques. It was found that the ratio between the two CTFs strongly depends on the spatial frequency. Low object frequencies provide much higher signals in EI than in FSP, which is due to FSP being to first approximation sensitive to the second derivative of the phase, rather than to the first derivative such as EI. Moreover, at high spatial frequencies the CTF tends to zero faster in FSP than in EI. At intermediate frequencies, the ratio between the two CTFs can assume values smaller or higher than 1, depending on the experimental parameters of the setup. In particular, the effect of the setup spatial resolution, driven by the detector and source blurring, is particularly strong. While the EI CTF is independent of the detector pixel size and decreases slowly with increased source blurring, FSP is very sensitive to changes in both quantities, with a sharp decrease of the signal at low resolutions. It thus appears that, provided a detector with a small pixel size and a source with a very small focal spot are available, the FSP technique can provide better results when high resolutions are needed (such as for small samples/details), while EI seems to be better suited for low/moderate resolutions (typically corresponding to larger samples/details).

Besides being useful for predicting the performance and frequency response of different EI and FSP setups, we believe this formalism could also form the basis of novel phase retrieval algorithms aimed at extracting object variations on a scale smaller than the size of the aperture. Future work will be dedicated to this subject.

Table 1. Glossary.

a : size of the aperture in the sample mask
 d : size of the aperture in the detector mask
 z_2 : sample-to-detector distance
 M : geometrical magnification
 z_{def} : defocusing distance
 y_e : position of the lower edge of the detector aperture
 p : sample scan position
 $\mathcal{G}_{s,p}$: source intensity distribution projected onto the detector plane
 $\mathcal{G}_{s,r}$: projected source intensity distribution rescaled back to the object plane
 \mathcal{g}_{ap} : function defining the smoothing of the edge transmission function
 \mathcal{g}_d : function defining the detector blurring
 $\mathcal{g}_{d,r}$: function defining the detector blurring, rescaled back to the object plane
 f_{det} : point-spread function of the detector, including both blurring from detector components and pixel binning.
 $f_{s,d}$: combined source-detector point-spread function referred to the object plane coordinates
 f_T : transmission sensitivity function
 f_R : refraction sensitivity function
 F_T : integral sensitivity function for transmission signal
 F_R : integral sensitivity function for refraction signal
 I_C : illumination curve

Acknowledgments

This work was supported by the UK Engineering and Physical Sciences Research Council (Grants EP/I021884/1 and EP/I022562/1). PCD is supported by a Marie Curie Career Integration Grants PCIG12-GA-2012-333990 within the Seventh Framework Programme of the European Union.